LANGMUIR

pubs.acs.org/Langmuir Article

Ag and Au Nanoparticles as Color Indicators for Monomer/Micelle–Nanoparticle Interactions

Prabhjot Kaur, Jaspreet Kaur Rajput, Kultar Singh, Poonam Khullar, and Mandeep Singh Bakshi*

Cite This: *Langmuir* 2022, 38, 7802–7814 Read Online

ACCESS | Metrics & More | Article Recommendations | Supporting Information

ABSTRACT: Ag and Au nanoparticles (NPs) were used as color indicators to determine the monomer/micelle adsorption on the NP surface. A simple methodology based on the color change of Ag/Au NPs upon interacting with surface-active molecules was developed. A contrasting color change occurred when NPs interact with the monomer/micelle. This was demonstrated by monitoring the adsorption behavior of a series of Gemini surfactants. UV–visible measurements showed a large change in the intensity and wavelength of Ag/Au NP absorbance upon the surface adsorption of the monomer/micelle of Gemini surfactants. The mechanism of surface adsorption and molecular orientation on the solid–liquid interface of NPs was determined by performing the FT-IR and XPS measurements. Results demonstrated that sharp color changes from yellow to red for Ag NPs and red to purple for Au NPs happened when the Gemini surfactant monomer/micelle adsorbs on the NP surface. This colorimeter-based methodology highlighted the applicability of Ag/Au NPs in complex media where such NPs frequently encounter surface-active molecules.

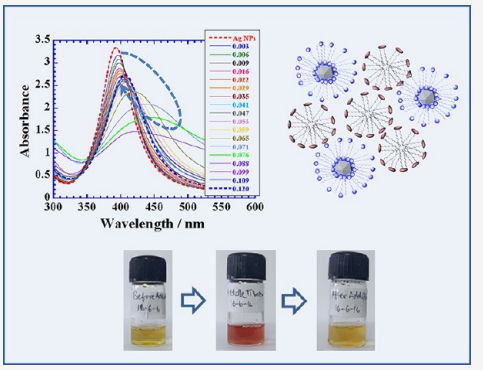

INTRODUCTION

Ionic surfactants are known for their shape-controlled synthesis of noble metal nanomaterials, which is governed by the solid–liquid interface adsorption of surfactant molecules.[1−4] Surface adsorption of surfactant molecules provides colloidal stabilization as well as shape-controlled crystal growth.[5,6] It happens due to the preferential adsorption of surfactant molecules on {100}/{110} rather than on {111} crystal planes of face-centered cubic (fcc) geometry, which restricts the availability of {100}/{110}, thereby leaving {111} crystal planes to produce anisotropic morphologies.[7,8] This process is very well accomplished when the concentration of the surfactant is much higher than its critical micelle concentration (cmc). The presence of the micellar phase during the crystallization growth kinetics plays an important role in the appropriate solid–liquid interface adsorption of surfactant molecules.[7] It makes available enough surfactant molecules for preferential surface adsorption through specific interactions on different crystal planes, thus driving the shape-controlled growth of the nucleating centers into desired morphologies. In this process, both hydrophilic and hydrophobic functional groups of surfactants play an important role.[7] Stronger hydrophilicity ensures effective surfactant binding on the crystal lattice, whereas stronger hydrophobicity produces a compact surfactant double-layer coating that passivates the crystal plane from participating in further growth process.[9−11] This dual property is very well demonstrated by the Gemini surfactants,[12−14] and hence, they prove to be better shape-directing agents in comparison to their conventional monomeric homologues. In this work, we exploit the surface adsorption of Gemini surfactants on tiny Ag/Au nanoparticles (NPs) to understand the solid–liquid interface adsorption as well as micelle formation by using the surface plasmon resonance (SPR) of Au/Ag NPs as an indicator. Although dyes are the common color indicators for tracing the micellar properties,[11,15] the use of Ag and Au NPs as color indicators provides an additional advantage to understand the adsorption of the monomer/micelle on the solid–liquid interface.

Ag/Au NPs depict the absorbance due to SPR in the visible region, which is highly sensitive to the colloidal nature of NPs. It is significantly affected by the surfactant adsorption on the NP surface that induces a strong influence on SPR, which in turn is reflected by the variation in intensity as well as wavelength.[15−17] Thus, both latter parameters act as strong indicators of the surfactant–NP interactions as well as micelle formation behavior of the surfactant in the presence of NPs. These properties are important to understand the appropriate applicability of Ag/Au NPs in complex media where NPs frequently encounter the presence of surface-active molecules and their aggregated assemblies.[18,19] We demonstrate this by

Received: April 2, 2022
Revised: May 3, 2022
Published: June 16, 2022

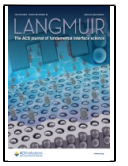

https://doi.org/10.1021/acs.langmuir.2c00853
Langmuir 2022, 38, 7802–7814

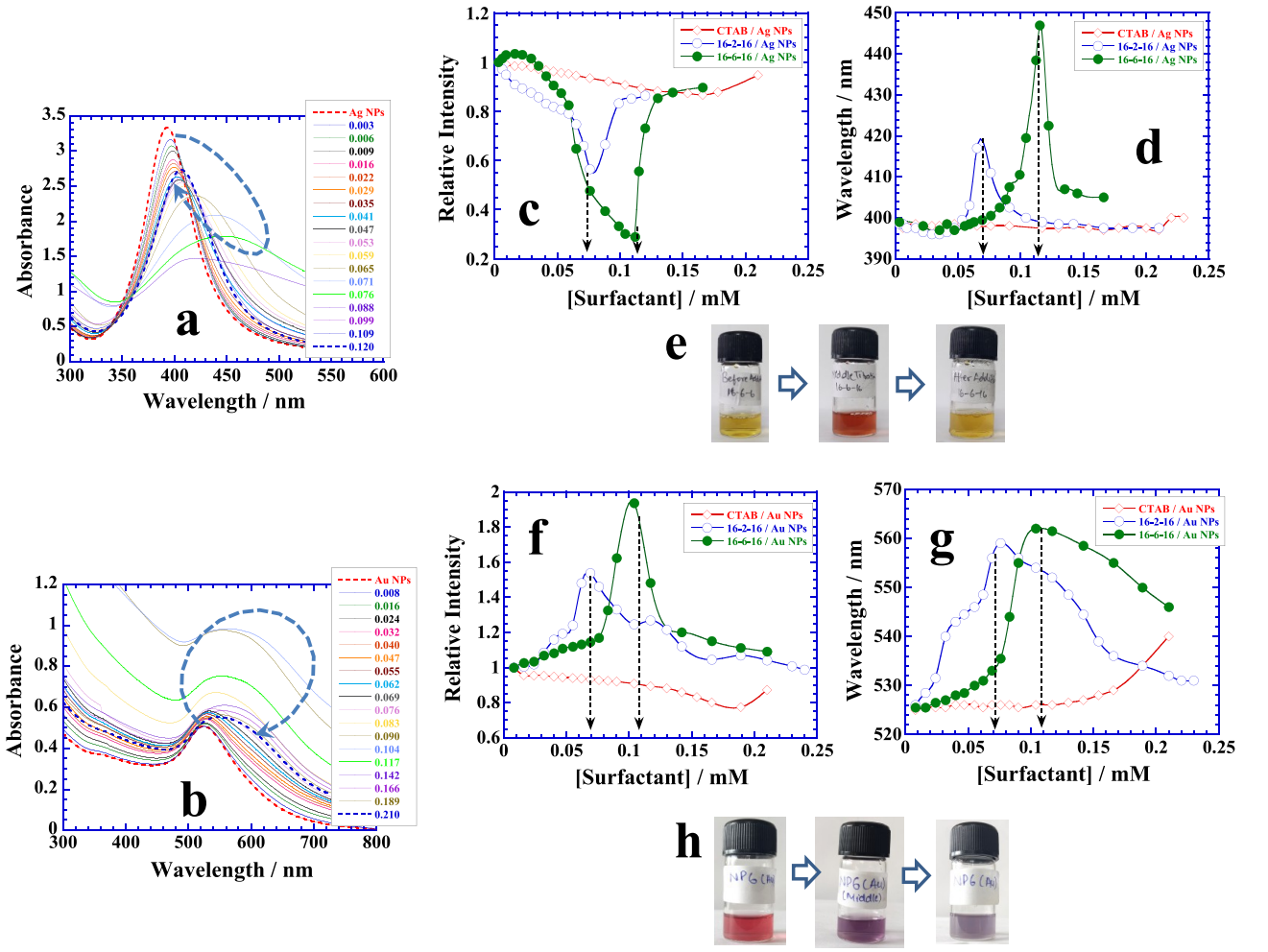

Figure 1. (a) UV−visible scans of a titration of 16-6-16 with a colloidal suspension of Ag NPs at 70 °C. The absorbance close to 400 nm belongs to Ag NPs. The dotted arrow shows the variation in the absorbance with respect to the concentration of 16-6-16. Each addition is carried out after a constant interval of time of 4 min so that the random time effect is excluded. (b) Similar UV−visible scans with Au NPs. (c, d) Plots of variation in the intensity and wavelength of absorbance of Ag NPs upon titrating with CTAB, 16-2-16, and 16-6-16. (e) Sample photos of the color change during the titration of 16-6-16 with Ag NPs. Note the color change from light yellow to dark red and back to light yellow during the titration. (f, g) Plots of variation in the intensity and wavelength of absorbance of Au NPs upon titrating with CTAB, 16-2-16, and 16-6-16. (h) Sample photos of the color change during the titration of 16-6-16 with Au NPs. Note the color change from red to dark purple and then to light purple during the titration.

choosing a series of highly surface-active Gemini surfactants whose micelle formation and solid−liquid interfacial behavior significantly depend on the head group as well as hydrocarbon tail modifications. The strong surface activity of Gemini surfactants stems from the dimeric ionic nature of the head group and highly hydrophobic nature of double-hydrocarbon chains. This dual combination of polar and nonpolar functional groups makes Gemini surfactants highly surface-active and drives their solid−liquid interface adsorption. Thus, Gemini surfactants are considered to be the best model amphiphiles of complex media[20−22] where noble metal NPs are frequently employed for diverse applications.

EXPERIMENTAL SECTION

Materials. Silver nitrate ($AgNO_3$), chloroauric acid ($HAuCl_4$), sodium dodecylsulfate (SDS), cetyltrimethylammonium bromide (CTAB), octyl-β-D-glucopyranoside (OGP), and *n*-dodecyl-β-D-maltoside (DDM) were purchased from Aldrich. Gemini surfactants dimethylene- (16-2-16), trimethylene- (16-3-16), tetramethylene- (16-4-16), pentamethylene- (16-5-16), and hexamethylene bis-(hexadecyldimethylammonium bromide) (16-6-16), α,ω-bis(3-tetradcylimidazolium-1-yl) ethane bromide (C14S2), -propane bromide (C14S3), and -butane bromide (C14S4) (where "S" stands for the methylene group), and 1,1′-(1,2-diemethylenethio)bis[1-methyl-3-(2-dodecyl)imidazolium] dibromide (12-2-S-2-12), -(2-tetradecyl)-imidazolium] dibromide (14-2-S-2-14), and -(2-hexadecyl)-imidazolium] dibromide (16-2-S-2-16) (where "S" refers to the thio functional group) were synthesized as reported elsewhere.[17−21] All Gemini surfactants were repeatedly purified from ethanol before use. Table S1 lists the cmc value of each surfactant. Molecular structures of different categories of surfactants used are shown in Figure S1. Double-distilled water was used for all preparations.

Methods. *Ag and Au NPs as Indicators.* Ag NPs were synthesized as a light yellow-brown suspension by taking [$AgNO_3$] = 0.25 mM and stabilizer [SDS] = 0.25 mM in 20 mL of total aqueous solution followed by the addition of 0.3 mL of ice-cold aqueous $NaBH_4$ ([$NaBH_4$] = 0.1 M) solution under constant stirring at room temperature.[12,23] The use of equal amounts of both $AgNO_3$ and SDS is to allow a maximum amount of SDS for colloidal stabilization of Ag NPs while leaving a minimum amount in the aqueous bulk because 0.25 mM is a much lower concentration than the cmc of SDS (Table S1). A similar reaction produced a ruby red suspension of Au NPs by using $HAuCl_4$. The samples were kept in the dark for at least 1 h

https://doi.org/10.1021/acs.langmuir.2c00853
Langmuir 2022, 38, 7802−7814

before use to provide maximum colloidal stability. Both suspensions were titrated with stock solutions of Gemini surfactants at precise 70 °C to understand the monomeric and micellar phase interactions with NPs. The purpose of choosing 70 °C was simply to get better and prominent results, which are usually not expected at low temperature. All experiments were simultaneously monitored with different techniques.

Characterization. UV−visible measurements were performed by using a Shimadzu-Model No. 2450 double-beam instrument, which was equipped with a TCC 240A thermoelectrically temperature-controlled cell holder that allowed one to measure the spectrum at a constant temperature within ±1 °C. Multi-angle particle sizing and low-angle zeta potential analyses were done by using dynamic light scattering (DLS) and electrophoretic light scattering (ELS), respectively, with a minimum number of optical components in an apparatus (NICOMP Nano Particle Size Analyzer system, model Z3000 ZLS). It was equipped with a Peltier thermoelectric element, which regulated the temperature of the sample cell within ±0.2 °C with a lower limit of 0 °C and an upper limit of 90 °C. Particle size analysis was calibrated with nanosphere size standards of 90 and 240 nm and recorded for both the Gaussian system and NICOMP distribution, while zeta potential was calibrated using zeta reference standards. All measurements were made using a quartz cuvette with a path length of 1 cm. Infrared absorption measurements were recorded with an FT-IR spectrometer (Shimadzu) in the range of 4000−400 cm^{-1}. Each spectrum was measured in transmission mode with 256 scans and 4 cm^{-1} resolution. The surface chemical composition of NPs was confirmed with the help of X-ray photoelectron spectroscopy (XPS) measurements. For the XPS analysis, Ag and Au NP samples were properly purified from pure water to remove the free surfactant so that the chemical composition of the surface-adsorbed surfactant on NPs could be determined accurately. Each sample was analyzed by using a Kratos Axis Ultra X-ray photoelectron spectrometer. XPS can detect all elements except hydrogen and helium and can probe the surface of the sample to a depth of 7−10 nm. Survey scan analyses were carried out with an analysis area of 300 μm × 700 μm. The shape and size of NPs were characterized by transmission electron microscopy (TEM). Samples were prepared by mounting a drop of a sample on a carbon-coated Cu grid and were allowed to dry in air. The experiments were performed with a JEOL 2010F field emission gun (FEG) operated at 200 kV.

RESULTS AND DISCUSSION

SPR Response of Ag/Au NPs as an Indicator. *Tetraalkylammonium Gemini Surfactants.* The first category of Gemini surfactants tested for surfactant−NP interactions is the derivatives of tetraalkylammonium bromide, which possess strong solid−liquid interface adsorption on the noble metal NP surface.[12,23,24] Their micellization behavior is compared with that of CTAB because CTAB is a monomeric homologue of Gemini surfactants and is the most versatile surfactant frequently used for the shape- and size-controlled synthesis of noble metal NPs.[25,26] Figure 1a,b shows UV−visible titrations of Ag and Au NP suspensions with an aqueous solution of 16-6-16, respectively. The initial absorbance of pure Ag and Au NPs is sharp. It becomes broad and red-shifts as the color change appears during the course of titration and again reverts to the original shape. The sharp absorbance is related to the SPR of individual monodisperse NPs in the aqueous phase, whereas the broad and red-shifted absorbance is usually due to the NP−NP interactions and is the consequence of self-aggregation among NPs.[7,8] A unique behavior is observed where a decrease in the intensity of Ag NPs and an increase in the intensity of Au NPs along with a red shift happen upon the addition of the surfactant before reverting close to their respective initial values (see dotted circular arrows in each figure). This is more prominent for 16-6-16 than 16-2-16 and the least for CTAB (Figure S2). Since the amount of NPs is constant, the increasing amount of the surfactant simply induces the micellization in the aqueous phase, which affects the surfactant adsorption on the NP surface. The latter effect alters the colloidal properties of NPs, which are reflected in the variation of the intensity and wavelength of Ag and Au NPs (Figure 1c,d and Figure 1f,g, respectively). The intensity passes through a strong minimum for Ag NPs (Figure 1c) and maximum for Au NPs (Figure 1f), whereas the wavelength in both cases (Figure 1d,g) produces a strong maximum. A red shift of ∼50 nm in both cases results in the contrasting color change of Ag NP suspension from light yellow to bright red and that of for Au NPs from red to purple before reverting to their original colors, which is quite clear in the former rather than in the latter case (see respective sample photos in Figure 1e,h). The color change produces highly stable suspensions and no NPs settle at the bottom in both cases. This unique and contrasting behavior between Ag and Au NPs is the most pronounced with 16-6-16, followed by 16-2-16, and is the least with CTAB, indicating a significant spacer effect on monomer/micelle−NP interactions.

The origin of this remarkable behavior is related to the SPR response of colloidal NPs upon their interactions with micelles in the aqueous phase. The absorbance at 400 nm of Ag NPs (Figure 1a) and at 520 nm of Au NPs (Figure 1b) in the absence of the Gemini surfactant is due to the SPR of individually dispersed NPs in aqueous bulk. Addition of the Gemini surfactant promotes its solid−liquid interface adsorption[27,28] on the Ag/Au NPs surface, which affects SPR. Surprisingly, the SPR response is completely opposite in both cases.[29] Surface adsorption of the Gemini surfactant on Ag NPs screens SPR, whereas it promotes that of Au NPs with the resulting intensity passing through a strong minimum (Figure 1c) and maximum (Figure 1f), respectively. More importantly, the minimum (Figure 1c) and maximum (Figure 1f) are appearing at the same concentration of the surfactant, i.e., 16-2-16 = 0.072 mM and 16-6-16 = 0.11 mM in both cases, but higher than the respective cmc values of 0.02 and 0.043 mM in pure water (Table S1). These values are termed as the critical aggregation concentration, cac, where stable micelle−NP aggregates are produced in the aqueous phase and are also listed in Table S1. The cac value denotes the "end point" here just like the one usually represented in conventional titrations leading to a marked color change. The identical values of cac in both cases indicate that the amount of surfactant adsorbed on Ag or Au NPs remains the same, which is fully supported by the identical variation of wavelength profiles (Figure 1d,g). But the contrasting variation in intensity (i.e., Figure 1c,f) is the consequence of the mode of surfactant adsorption on Ag and Au NP surfaces, which is due to the opposite plasmon-induced photoelectric effect of Ag and Au NPs of the same shape and size.[29,30] This directional charge transfer behavior, which originates from the plasmoelectric potential effect, allows the electrons to exit from the Ag NPs, while they enter into the Au NPs.[31] It promotes the stronger adsorption of the cationic Gemini surfactant on Ag NPs rather than on the Au NP surface. The stronger adsorption results in the formation of a compact bilayer on the Ag NP surface, which effectively passivates the surface, impeding the resonance effect of a free electron cloud with incoming light photons. On the other hand, the increase in intensity in the case of Au NPs is usually associated with colloidal stabilization[16,17] that reduces the NP−NP interactions and hence promotes the SPR. Interest-

https://doi.org/10.1021/acs.langmuir.2c00853
Langmuir 2022, 38, 7802−7814

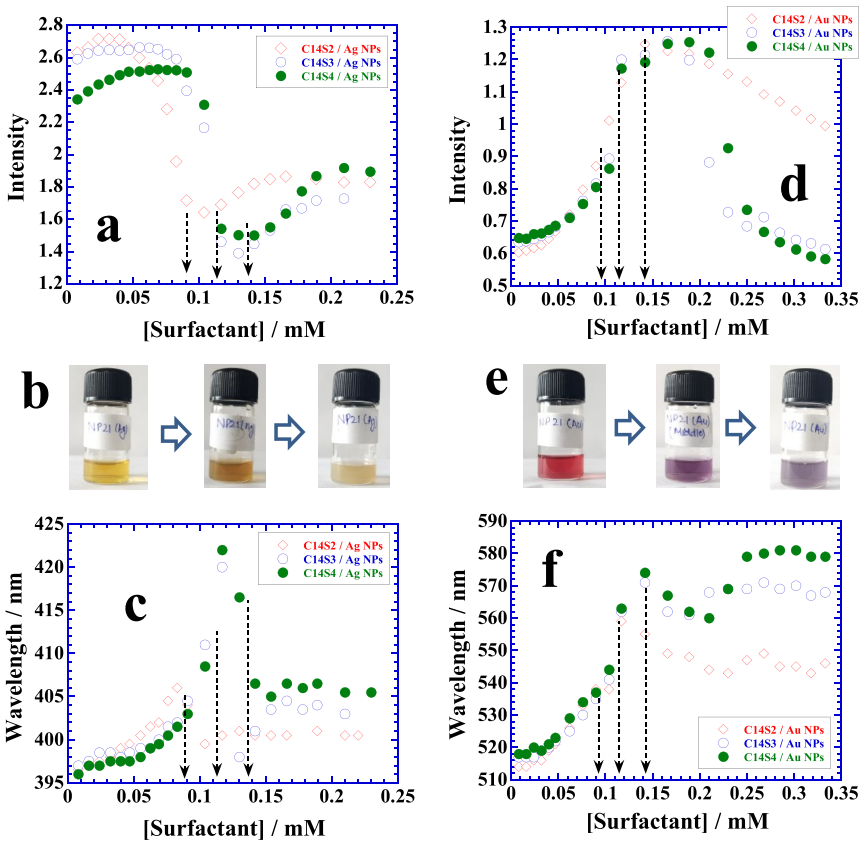

Figure 2. (a, c) Plots of variation in the intensity and wavelength of absorbance of Ag NPs upon titrating with C14S2, C14S3, and C14S4. (b) Sample photos of the color change during the titration of C14S4 with Ag NPs. Note the color change from bright yellow to yellow brown and back to light yellow during the titration. (d, f) Plots of variation in the intensity and wavelength of absorbance of Au NPs upon titrating with C14S2, C14S3, and C14S4. (e) Sample photos of the color change during the titration of C14S4 with Au NPs. Note the color change from red to dark purple and then to light purple during the titration.

ingly, both contrasting factors equally depend on the spacer effect and increase with the increase in spacer length (Table S1).

Imidazolium Gemini Surfactants. Similar contrasting behavior among the SPR responses of Ag and Au NPs is observed when, instead of tetraalkylammonium, imidazolium surfactants are used (Figure 2). Again, the intensity shows a shallow minimum for Ag NPs (Figure 2a), whereas a pronounced maximum is observed for Au NPs (Figure 2d). Both intensity and wavelength variations show a clear spacer effect for C14S2, C14S3, and C14S4 (Figure S3 for Ag NPs and Figure S4 for Au NPs). The cac values (dotted arrows in each case) thus obtained from the intensity and wavelength profiles agree with each other as well as for Ag and Au NPs and increase with spacer length as noted previously (Table S1). Imidazolium surfactants with the thio ether (−S−) spacer functional group, i.e., 12-2-S-2-12, 14-2-S-2-14, and 16-2-S-2-16, are also tested (Figure S5 for Ag NPs and Figure S6 for Au NPs). The thio functional group is expected to have much stronger interactions with Ag/Au nanometallic surfaces. It causes a clear departure from the shallow minimum (Figure 2a) to the sign curve of intensity (Figure 3a), indicating a much stronger adsorption of the *n*-S-2-S-*n* surfactant in comparison to that of C14Sn on the Ag NP surface. In the sign curve, there is no tendency for the absorbance to revert to its original value because all incoming *n*-S-2-S-*n* molecules tend to complex with Ag NPs. This is not the case with Au NPs where the intensity passes through a strong maximum, thus further discriminating the plasmoelectric potential effect among the Ag and Au NPs. The cac values obtained (dotted arrows in Figure 3) are also listed in Table S1.

Finally, we treat Ag/Au NP suspensions with non-ionic ORG and DDM (Figure S7) to demonstrate the fact that solid−liquid interface adsorption on nanometallic surfaces is mainly facilitated by the ionic surfactants rather than the non-ionic surfactants. The presence of the ORG/DDM monomer/micelle does not depict a similar change in the intensity or wavelength profiles of Ag/Au NPs within the comparable concentration range (Figure S8) as observed for ionic surfactants, hence showing little monomer/micelle−NP interactions. Although both ORG and DDM are water-soluble non-ionic surfactants that contain polar functional groups in their head group region (Figure S1), the low polarity and bulkiness of their head groups induce steric hindrances for an effective solid−liquid interface adsorption.

Aggregation and cac. Size and zeta potential (ζ) studies are the most appropriate quantitative measurements for exploring the aggregation behavior of ionic surfactants[32,33] as well as their adsorption on Ag/Au NPs. Figure 4 shows the size and ζ profiles of adsorption of 16-2-16/16-6-16 on Ag and Au NPs. Similar results for imidazolium surfactants are shown in Figure S9. The variation is identical in Figure 4a−c for Ag and Au NPs despite the opposite variation of intensity in Figure 1c,f. For both kinds of NPs, the size and ζ become maximally close to cac before reverting to the original value, supplementing our earlier discussion that cac is the

https://doi.org/10.1021/acs.langmuir.2c00853
Langmuir 2022, 38, 7802−7814

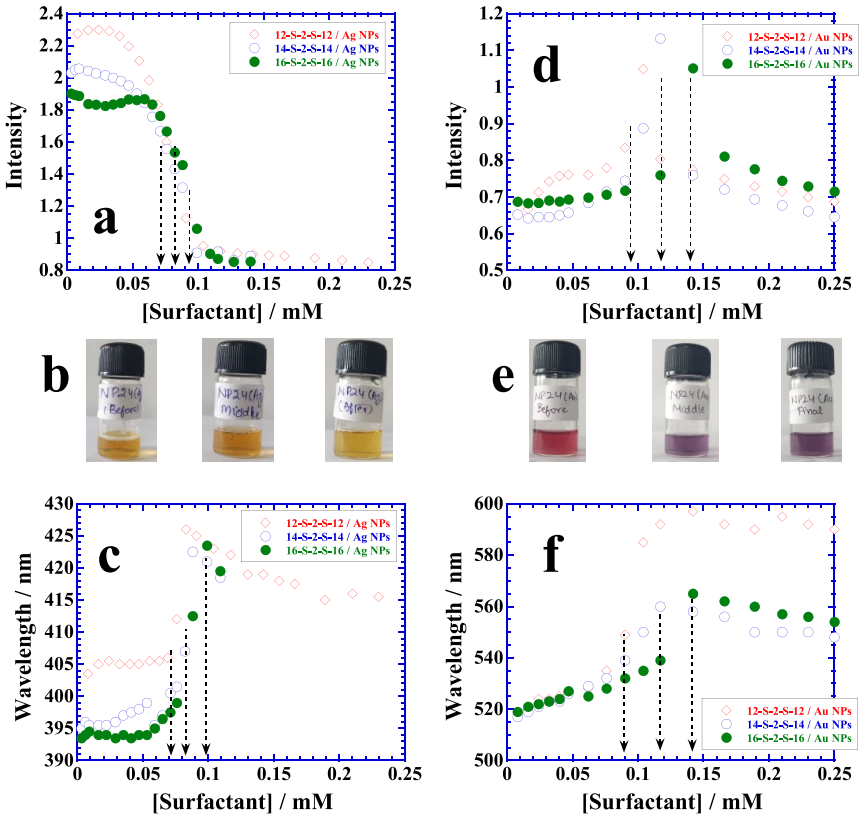

Figure 3. (a, c) Plots of variation in the intensity and wavelength of absorbance of Ag NPs upon titrating with 12-S-2-S-12, 14-S-2-S14, and 16-S-2-S-16. (b) Sample photos of the color change during the titration of 16-S-2-S-16 with Ag NPs. Note the color change from bright yellow to deep yellow and back to bright yellow during the titration. (d, f) Plots of variation in the intensity and wavelength of absorbance of Au NPs upon titrating with 12-S-2-S-12, 14-S-2-S14, and 16-S-2-S-16. (e) Sample photos of the color change during the titration of 16-S-2-S-16 with Au NPs. Note the color change from red to light purple and then to dark purple during the titration.

consequence of monomer/micelle adsorption on the NPs surface. Both SDS-stabilized Ag NPs (Figure 4a) and Au NPs (Figure 4c) exhibit less than 50 nm size in the absence of the Gemini surfactant. Addition of the Gemini surfactant leads to a gradual increase in size, which becomes highly prominently close to cac. Likewise, the ζ value of Ag NP (Figure 4b) and Au NP (Figure 4d) suspensions is less than −50 mV, which remains more or less constant upon the addition of the cationic Gemini surfactant but becomes significantly positive[34,35] and reaches close to 250 mV at cac. Such a huge increase in ζ is due to the formation of large positively charged aggregates whose charge density is much higher for 16-2-16/16-6-16 in comparison to that produced by CTAB. Both the size and ζ indicate that the adsorption of the Gemini surfactant on Ag and Au NP surfaces takes place in an identical manner in contrast to the opposite variation of intensity depicted in Figure 1c,f, respectively. Thus, the opposite variation of intensity is happening only due to the opposite plasmon-induced photoelectric effect of Ag and Ag NPs.

cac and Surfactant Molecular Structure. Figure 4e shows the relationship between the molecular structure of the Gemini surfactant and the cac. The cac varies linearly with spacer length. The micellar behavior of the ionic surfactant is significantly affected by the head group modification.[36,37] The bulky ionic head group or introduction of the nonpolar methylene spacer in the head group region usually leads to the delay in the micelle formation, which is also reflected in Figure 4e with spacer length. At a fixed spacer length (dotted arrow in Figure 4e), imidazolium produces a higher cac than alkylammonium Gemini surfactants. However, the cac drops significantly when a thio ether spacer is introduced in the imidazolium head group (e.g., compare cac between C14S4 and 16-S-2-S-16 in Figure 4e). Solid−liquid interface adsorption is facilitated by the strong binding of the thio ether spacer group on the Ag/Au NP surface, which promotes the self-aggregation among the micelles and NPs. A shorter hydrocarbon chain further helps in the surface adsorption by reducing the overall nonpolarity of the surfactant molecule, which in turn promotes the surface adsorption and leads to a further decrease in cac (Figure 4e).

Morphology of Surfactant−NPs. Microscopic analysis illustrates the shape and size of the Ag/Au NPs and their mode of aggregation. Figure 5a−d supports the surfactant adsorption on the NP surface and compares the adsorption of 16-2-16 on Ag and Au NPs, respectively. In both cases (Figure 5a,c), roughly spherical NPs of less than 50 nm undergo a high degree of self-aggregation caused by the surface adsorption of the Gemini surfactant, which is in fact the consequence of the large size depicted in Figure 4a,c. Self-aggregation also promotes the interparticle fusions (see black arrows in Figure 5b,d), but most of the NPs are well separated by a thin surfactant coating, which is not the outcome of an image artifact under a high-intensity electron beam. Such large aggregates in the colloidal state produce a large value of ζ for both kinds of NPs in Figure 4b,d. Similarly, TEM images of Figure 5e−h belong to Ag NPs in the presence of C14S2 and 16-S-2-S-16. Although a similar kind of aggregation behavior is observed, interparticle fusions are more prevalent, which

https://doi.org/10.1021/acs.langmuir.2c00853
Langmuir 2022, 38, 7802−7814

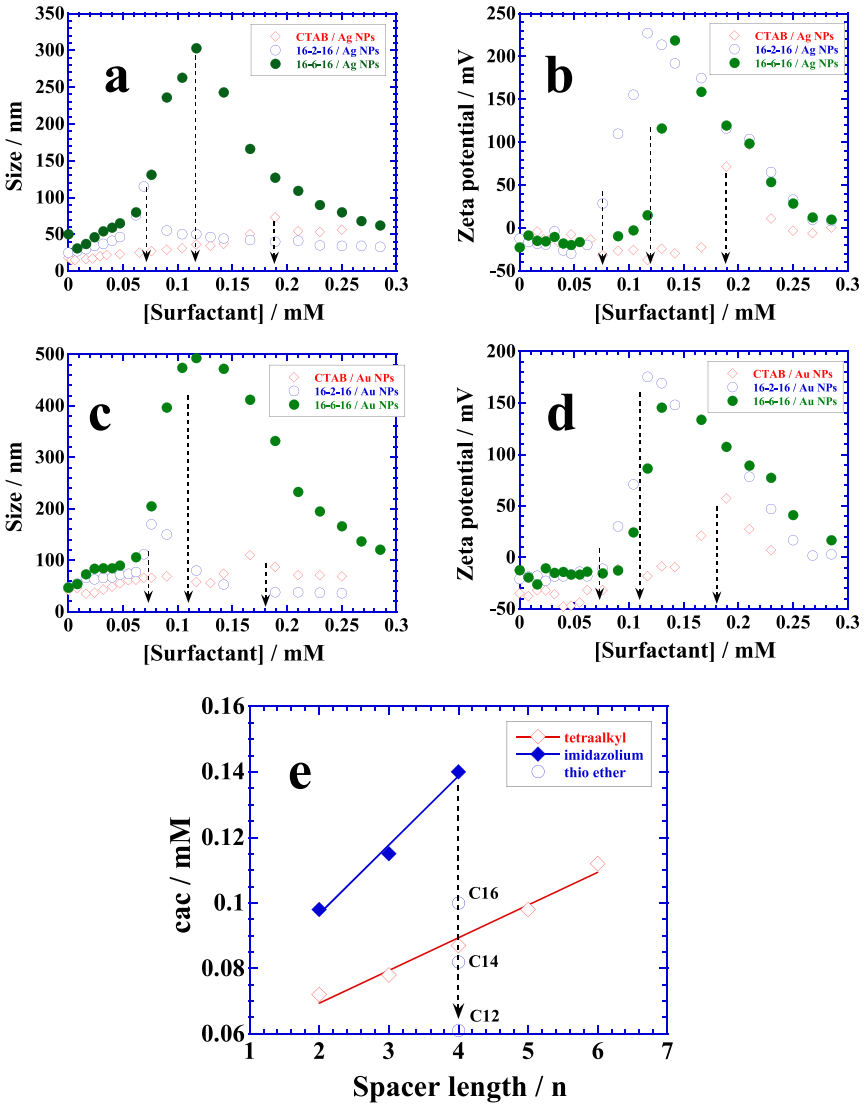

Figure 4. (a, b) Plots of variation in the size and ζ of Ag NPs upon titrating with CTAB, 16-2-16, and 16-6-16. (c, d) Plots of variation in the size and ζ of Au NPs upon titrating with CTAB, 16-2-16, and 16-6-16. (e) Plots of variation in cac with spacer length for different Gemini surfactants.

produce NPs of larger dimensions. A smaller cac than the respective cmc value of both surfactants (Table S1) seems to be the contributing factor that allows less number of surfactant molecules to adsorb on the NP surface, thus leaving some of the crystal planes of fcc geometry unpassivated. The uncoated crystal planes are the active sites for the NP−NP interactions and hence produce NPs of larger dimensions. On the other hand, when the cac is larger than the cmc as in the case of 16-2-16/16-6-16 (Table S1), adsorption of a greater amount of surfactant in the form of micelles rather than the monomers is expected to occur on the NP surface. It generates a thick coating of micellar phase, which passivates different crystal planes of fcc geometry from further participation in crystal growth and hence provides a stronger energy barrier for NP−NP fusions (Figure 5b,d). Furthermore, the microscopic analysis does not differentiate between the modes of Gemini surfactant adsorption and aggregation behavior on Ag and Au NP surfaces because it is carried out in the dried state.

Modes of Surface Adsorption. Solid−liquid interfacial adsorption of surfactant molecules on the Ag/Au NP surface is best determined by the IR analysis. After each titration, surfactant-complexed NPs are centrifuged and purified from pure water to remove the uncomplexed surfactant and are analyzed (Figure 6a). SDS is a colloidal stabilizer for Ag/Au NPs; hence, it is already adsorbed on the NP surface. The vibrational frequencies of SDS-stabilized Ag/Au NPs are listed in Table S2 along with that of pure SDS. Surface-adsorbed SDS depicts the following prominent bands at 2955 cm^{-1} $(CH_3)_{as}$, 2873 cm^{-1} $(CH_3)_s$, 2917 cm^{-1} $(CH_2)_{as}$, 2849 cm^{-1} $(CH_2)_s$, 1468 cm^{-1} $(CH_2)_{scis}$, 720 cm^{-1} $(CH_2)_{rock}$, 1341 cm^{-1} $(CH_2)_{wagg}$, 1084 cm^{-1} $(SO_2)_s$, and a doublet composed of 1219 and 1249 cm^{-1} $(SO_2)_{as}$. When this sample is treated with CTAB or 16-*n*-16 (spacer, n = 1−6), vibrational bands arising from the head group region of SDS (SO_2) and 16-*n*-16 are significantly affected because of the interactions between the oppositely charged head groups of SDS and CTAB/16-*n*-16 (Figure 6b). Such an orientation of the surfactant molecules (Figure 6c) leaves the vibrational bands of the hydrocarbon chain due to different alkyl groups largely unaffected, while that of $(CH_2)_{wagg}$ at 1341−1360 cm^{-1} completely disappears. It happens due to a change in the angle of atoms of the methylene group versus the plane of the SDS molecule in the event of compact bilayer formation among the hydrocarbon chains.[38,39] Since the interactions are happening through

https://doi.org/10.1021/acs.langmuir.2c00853
Langmuir 2022, 38, 7802−7814

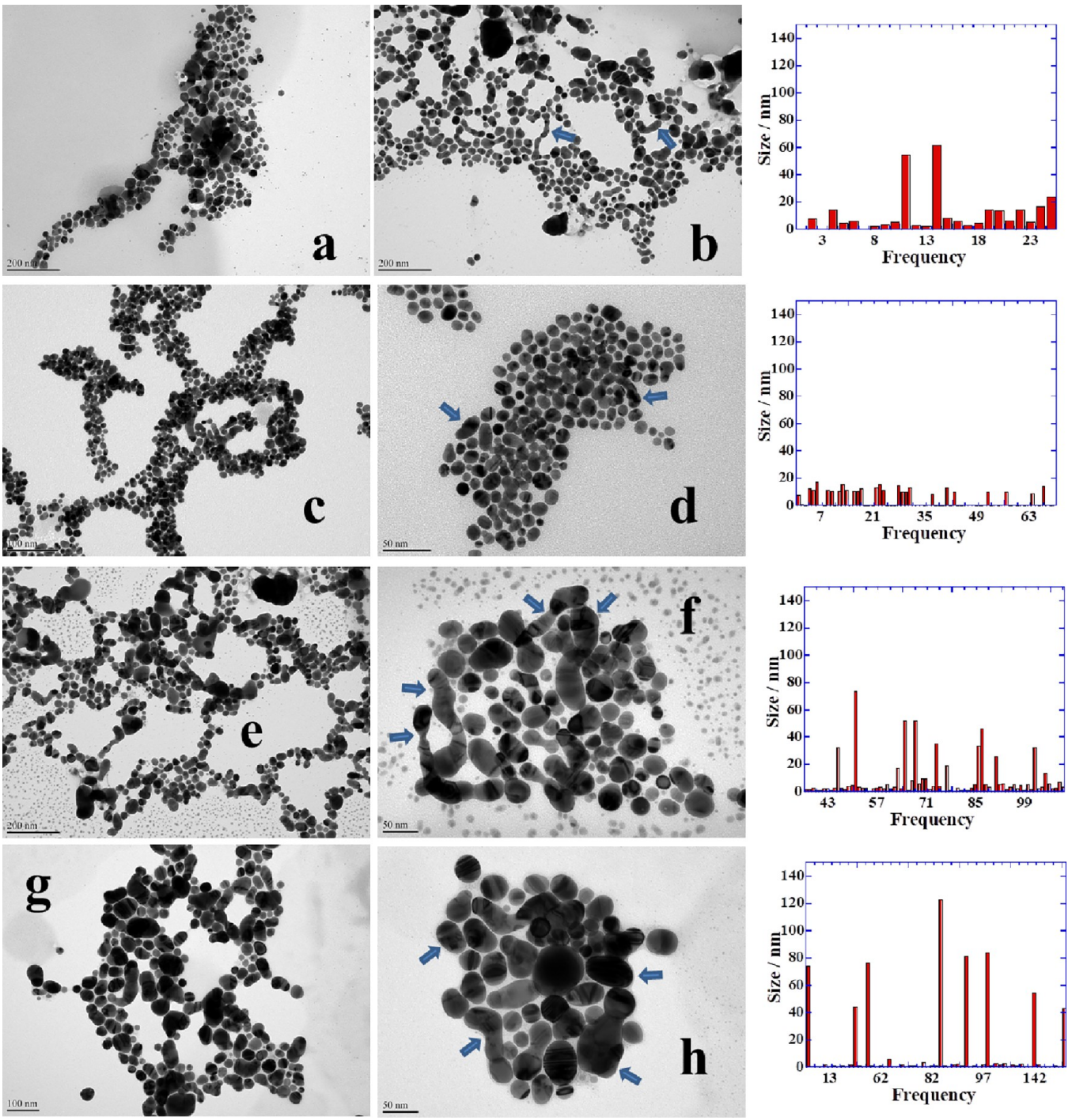

Figure 5. (a–d) TEM images of the 16-2-16 surface adsorbed on Ag (a, b) and Au NPs (c, d), respectively. Block arrows indicate the interparticle fusions in some cases. (e–h) TEM images of C14S2 (e, f) and 16-S-2-S-16 (g, h) surfaces adsorbed on Ag NPs, respectively. Block arrows indicate the interparticle fusions in some cases. See details in the text.

oppositely charged head groups of SDS and 16-*n*-16, the frequency of the doublet of SDS (SO_2) depends on the spacer length of 16-*n*-16 (Figure 6b), which even merges into a single peak for 16-2-16 as well as 16-3-16, indicating much stronger adsorption due to a better compatibility between the SDS layer and the spacer length of two to three methylene groups of 16-*n*-16. The effect is minimum for CTAB, supplementing our earlier conclusion that surface adsorption of 16-*n*-16 is much stronger than that of CTAB. Such interactions cause a dramatic change in the head group vibrational frequencies of (N–$CH_3)_{as}$, (N–$CH_3)_s$, and (C–N) at around 3016, 1394, and 911 cm^{-1}, respectively. The vibrational bands of (N–$CH_3)_{as}$ and (C–N) disappear, while that of (N–$CH_3)_{as}$ shifts to higher frequency (Table S2), indicating a compact arrangement of the quaternary ammonium head group upon interacting with SDS molecules (Figure 6c).

Similar results are obtained for the imidazolium (C14S*n*) series of surfactants (Figures S10–S13). Although we do not see any change in the C–H stretching frequencies of $(CH_3)_{as}$, $(CH_2)_{as}$, $(CH_2)_s$, $(CH_2)_{scis}$, and $(CH_2)_{rock}$, the peaks due to

https://doi.org/10.1021/acs.langmuir.2c00853
Langmuir 2022, 38, 7802–7814

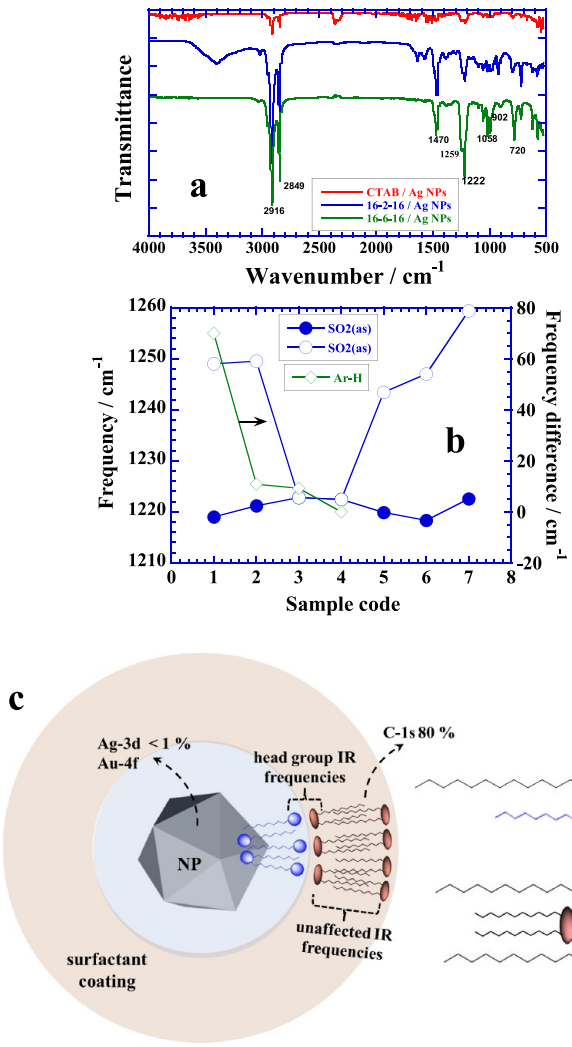

Figure 6. (a) FT-IR spectra of the CTAB/16-2-16/16-6-16 surface adsorbed on Ag NPs. Identification of vibrational bands is specified in Table S2. (b) Plots of variation of vibrational frequencies of SO_2(as) and Ar-H functional groups with the spacer length. Sample codes (circles) refer to the following samples: (1) SDS-stabilized Ag NPs, (2) CTAB adsorbed on Ag NPs, (3) 16-2-16, (4) 16-3-16, (5) 16-4-16, (6) 16-5-16, and (7) 16-6-16 adsorbed on Ag NPs. Sample codes (diamonds) for the following samples: (1) pure C14S2, (2) C14S2, (3) C14S3, and (4) C14S4 adsorbed on Ag NPs. (c) Schematic representation of SDS-stabilized NPs with a surface coating of 16-2-16 Gemini surfactants. Note the head group orientations as a result of oppositely charged interactions between SDS and 16-2-16 and bilayer formation by the double-hydrocarbon chains due to hydrophobic interactions. The label C-1s refers to 80% and Ag-3d/Au-4f refers to less than 1% atomic percent from XPS analysis. See details in the text.

$(CH_3)_s$, $(SO_2)_s$, and conjugated π-bonds at 2873, 1084, and 2050 cm^{-1}, respectively, completely disappear (Table S3). A doublet of Ar-H at 3106 and 3037 cm^{-1} with a frequency difference of 70 cm^{-1} shows a marked decrease with spacer length, and eventually, both peaks merge when n = 4 in the case of C14S4 (Figure 6b). It shows a significant involvement of the aromatic system of the imidazolium head group in association with SDS during the solid−liquid adsorption with the results showing that the vibrational band due to the π-bond at 2050 cm^{-1} disappears and that of C═N shows a marked decrease from 1688 to 1653 cm^{-1}.[40] The oppositely charged interactions between the imidazolium and SDS head groups even cause the C═C band frequency to increase from 1559 cm^{-1} for C14S2 to 1569 cm^{-1} for C14S4 with the spacer length (Table S3). As indicated by UV−visible studies, the surface adsorption becomes even much stronger when the thio ether functional group is introduced in the spacer of the imidazolium surfactant head group region. Such a strong adsorption mainly driven by the thio ether association on the Ag/Au NP surface completely eliminates the vibrational bands due to CN^+ and the conjugated π-bond and hence induces a complete merger of the doublet of $(SO_2)_{as}$ (Figures S14−S16 and Table S3).

Elemental Analysis of Surfactant-Adsorbed Ag/Au NPs. XPS analysis is used to determine the elemental composition of the Gemini surfactant adsorbed on Ag/Au NPs. The high-resolution spectra of C-1s, O-1s, S-2p, N-1s, and Ag-3d of a sample consisting of 16-2-16 adsorbed on the Ag NP surface in Figure 1a are shown in Figure 7, whereas the binding energies are listed in Table 1. The survey scan spectra of samples in Figure 1b (16-2-16/Au NPs), Figure 2a (C14S2/Ag NPs), and Figure 3a (16-S-2-S-16/Ag NPs) are presented in Figures S17−S20. Among all the important species, the major relative abundance of about 85% is contributed by C-1s of C−C and C−H functional groups,[41] which is the main source of single- and double-hydrocarbon chains of SDS and the Gemini surfactant, respectively, adsorbed on the NP surface (Figure 6c). There is a little difference between the relative abundance of C-1s among different samples (Table 1), indicating the fact that all Gemini surfactants show significant surface adsorption on Ag and Au NPs. The second largest contribution is provided by O-1s with a relative abundance close to 9%. Note a significantly less amount of O-1s in comparison to that of C-1s, which indicates the presence of a thick surface coating due to long double-hydrocarbon chains of Gemini surfactants. O-1s is mainly contributed by the sulfate groups of SDS, which are instrumental in creating a surfactant membrane on the NP surface with a binding energy close to 531 eV. XPS provides a characteristic peak of oxygen in surface sulfate around 531 eV, revealing that the NP surface is predominantly covered by sulfate species.[42,43] In all samples, the main contribution of O-1s is due to the surface-adsorbed sulfate species, but its amount is relatively much less than that of "O-1s lattice oxide" located around 530.1 eV[44] for 16-S-2-S-16/Ag NPs. It happens because of the much stronger surface adsorption of 16-S-2-S-16 due to the presence of thiol ether functional groups, which reduce the relative abundance of sulfate species.

XPS studies produce different species of S-2p with the overall relative abundance close to 2%. Among them, the contribution of sulfate species with a binding energy close to 168 eV[45] is the maximum, with a relative abundance of 66% in "16-2-16/Ag NPs" and "16-2-16/Au NPs" (Table 1). It decreases to 33% for "C14S4/Ag NPs" and "16-S-2-S-16/Ag NPs" due to their much stronger surface adsorption as depicted from UV−visible studies in Figures 2a and 3a, respectively. The "16-S-2-S-16/Ag NPs" surface-adsorbed sample also shows an additional relative abundance of 33% due to thio ether functional groups with binding energies at 162.9 and 164.1 eV and an area ratio of 2:1 representing the two spin−orbits.[46] This is in agreement with 163.5 eV assigned for the physisorbed thiols.[47] Since all Gemini surfactants possess either tetraalkylammonium or imidazolium head groups, the XPS analysis of N-1s with the overall relative abundance of 4% and binding energy close to 401 eV provides

https://doi.org/10.1021/acs.langmuir.2c00853
Langmuir 2022, 38, 7802−7814

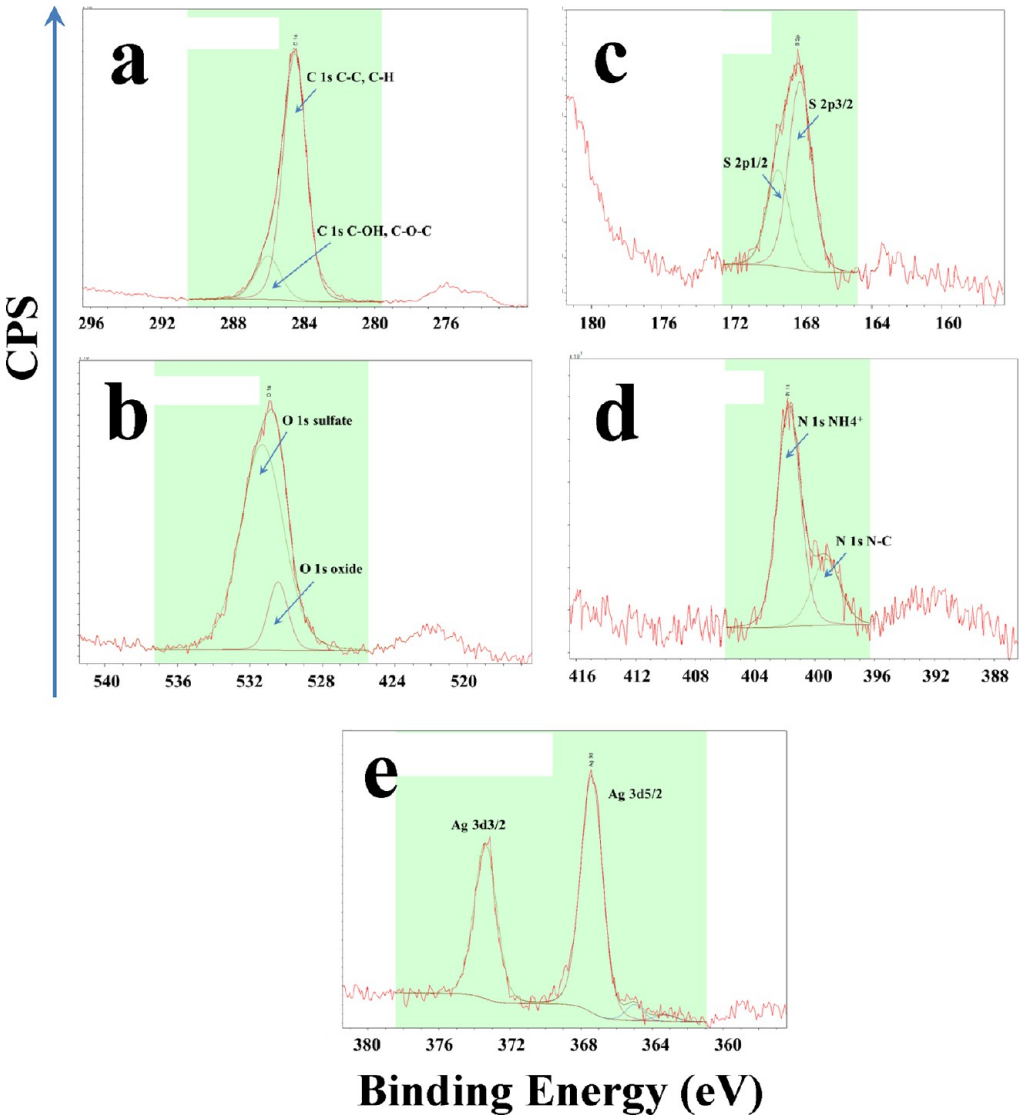

Figure 7. (a–e) High-resolution XPS spectra of C-1s, O-1s, S-2p, N-1s, and Ag-3d of the 16-2-16 surface adsorbed on Ag NPs. See details in the text.

valuable information about their surface adsorption. Two major species due to NH_4^+ with a binding energy of around 401 eV and a relative abundance of more than 70% and N–C with a binding energy close to 399 eV are observed.[48] Both represent the relative abundance of N-1s contributed by the head group region of Gemini surfactants (see Figure 6c), and it is the third highest among all the species studied.

The most significant part of this analysis is the overall relative abundance of both Ag-3d and Au-4f with binding energies of 368 and 83.5 eV, respectively, in their respective samples (Table 1). Both show less than or close to 1% relative abundance, which is the minimum among all species studied. The origin of such a low relative abundance is the presence of a thick blanket of Gemini surfactant coating on the Ag/Au NP surface (Figure 6c). Although XPS can analyze surface properties of about 10 nm in thickness, a relative abundance of less than 1% clearly indicates the presence of several layers of coating on the Ag/Au NP surface. Two species of Ag-3d, i.e., Ag-3d5/2 and Ag-3d3/2, appear around 367 and 373 eV, respectively, indicating the surface-bound SO_4 or –S– functional groups and the metallic nature of silver, respectively.[49] The relative abundance of the former is about 60%, whereas that of the latter is close to 40%. It shows that more than half of the nanometallic surface of Ag NPs is coated with SDS molecules that provide colloidal stabilization, whereas 40% of the nanometallic surface is devoid of SDS coating. On the other hand, the binding energies of Au-4f5/2 and Au-4f7/2 species located around 87.7 and 84.1 eV, respectively, correspond to the bulk Au[14] for "16-2-16/Au NPs" with a relative abundance of just 0.31%, which is the one-third equivalent of the Ag-3d sample. Such a low relative abundance of Au in comparison to that of Ag is due to the greater adsorption/aggregation of 16-2-16 on the Au NP surface rather than the Ag NP surface as observed earlier from the UV–visible studies where the purple color does not revert to the original red color (Figure 1h).

Mechanism. *Surface Adsorption.* Ag/Au NPs as indicators used in this study are stabilized with SDS to achieve colloidal stabilization. The amount of SDS used for this purpose is equal to the amount of metal salt used in the synthesis of Ag/Au NPs (see Experimental Section) to ensure that the maximum amount of SDS remains adsorbed on the NP surface for

https://doi.org/10.1021/acs.langmuir.2c00853
Langmuir 2022, 38, 7802–7814

Table 1. XPS Analysis of Surface-Adsorbed Gemini Surfactants on Ag and Au NPs[a]

		16-2-16/Ag NPs		16-2-16/Au NPs		C14S2/Ag NPs		16-S-2-S-16/Ag NPs	
	species	atomic %	area %	atomic %	area %	atomic %	area %	atomic %	area %
C-1s		85.4 (285.4)		84.7 (284.5)		83.5 (284.5)		83.6 (284.1)	
	C−C, C−H		84.3 (284.5)		85.9 (284.5)		81.7 (284.5)		81.0 (284.5)
	C−OH, C−O−C		15.6 (286.0)		14.1 (286.0)		18.2 (286.0)		18.9 (286.0)
O-1s		8.64 (531.4)		9.93 (531.5)		4.91 (400.5)		9.74 (530.1)	
	O-1s (adventitious)				13.31 (530.2)				
	O-1s (SO_4^{2-})		86.8 (531.3)		86.6 (531.1)		100.0 (530.7)		24.1 (531.6)
	O-1s (oxide)		13.2 (530.4)						75.8 (530.2)
S-2p		1.03 (168.4)		2.45 (168.5)		2.06 (168.5)		2.00 (168.1)	
	S-2p3/2 (SO_4^{2-})		66.6 (168.1)		66.6 (167.8)		33.3 (167.9)		33.7 (168.1)
	S-2p1/2		33.3 (169.3)		33.3 (169.1)		33.3 (169.1)		16.8 (169.2)
	S-2p3/2 (S−C)								32.9 (162.9)
	S-2p1/2 (−S−C)								16.45 (164.1)
N-1s		3.36 (401.7)		2.59 (401.5)		4.91 (400.5)		4.12 (400.1)	
	N-1s (NH_4^+)		73.3 (401.7)		76.3 (401.3)		71.6 (400.8)		76.3 (400.7)
	N-1s (organic N)		26.6 (399.2)		23.6 (398.6)		28.3 (399.4)		23.6 (398.8)
Ag-3d		0.85 (367.4)				1.16 (368.5)		0.46 (367.1)	
	Ag-3d5/2 (S)		60.1 (367.4)				60.1 (367.9)		60.1 (367.4)
	Ag-3d3/2		39.8 (373.3)				39.8 (373.8)		39.8 (373.4)
Au-4f				0.31 (83.5)					
	Au-4f7/2				57.2 (84.1)				
	Au-4fS/2				42.7 (87.7)				

[a]All binding energies/eV are listed in parentheses along with atomic % and area % entries.

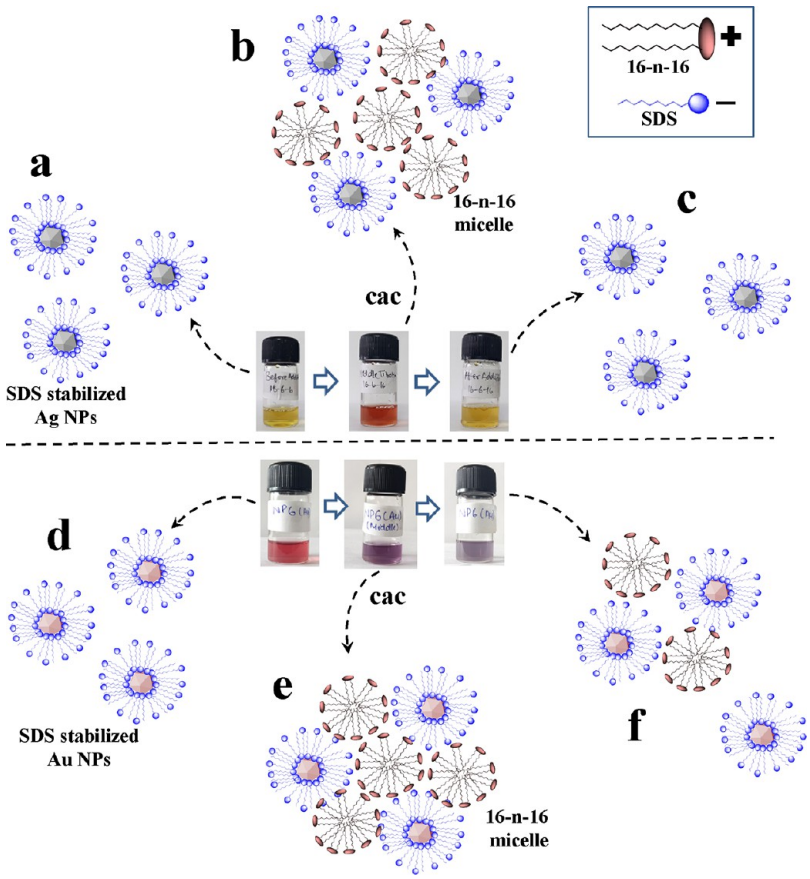

Figure 8. (a) SDS-stabilized Ag NPs. Adsorption of anionic SDS molecules on the NP surface takes place in the form of a bilayer so that polar head groups are in contact with the aqueous phase. (b) Interactions between anionic SDS-stabilized Ag NPs and cationic 16-*n*-16 micelles, leading to the self-aggregation at cac. (c) Desorption of 16-*n*-16 micelles from Ag NPs due to micelle transitions or micelle−micelle interactions, leading to a contrasting color change from yellow to deep red and back to yellow. 16-*n*-16 micelles are not shown in this part of the diagram. (d−f) Similar corresponding steps of the diagrams for anionic SDS-stabilized Au NPs. See details in the text.

https://doi.org/10.1021/acs.langmuir.2c00853
Langmuir 2022, 38, 7802−7814

colloidal stabilization. It provides ζ of less than −50 mV on both Ag NPs (Figure 4b) and Au NPs (Figure 4d) in aqueous suspensions that attract cationic Gemini surfactant molecules for surface adsorption. Usually, the NP surface is not expected to be entirely coated with SDS molecules because of the unequal preferences of different crystal planes of fcc geometry. XPS analysis (Table 1) indicates that about 60% of the Ag/Au NP surface is only occupied with SDS, leaving the rest available for the adsorption of Gemini surfactant molecules. The Gemini monomer/micelle mainly encounters SDS-stabilized Ag/Au NPs along with few free SDS molecules in aqueous bulk. That alters the SPR response of NPs (Figures 1−3) and consequently generates a contrasting color change in Ag NP (Figure 1e) and Au NP (Figure 1h) suspensions, making them potential indicators for surfactant−NP interactions. Figure 8 shows different steps of this mechanism. The surface-adsorbed bilayer of SDS molecules (Figure 8a) leaves anionic head groups in the aqueous phase for oppositely charged electrostatic interactions with the Gemini monomer/micelle (Figure 8b).

Color Change. In either case, Ag/Au NPs exhibit remarkable indicator behavior with a strong color contrast, which works well when micelles adsorb and desorb from the NP surface. Adsorption of micelles on Ag NPs brings several NPs in close vicinity that alters the SPR response and induces a sharp color change from yellow to red (Figure 8b). Desorption sets in at higher surfactant concentration where either micelle transitions or micelle−micelle interactions predominate and reverts the red color to yellow (Figure 8c). When adsorption is predominant over desorption as in the case of Au NPs (Figure 8d,e), some of the micelles remain associated with NPs (Figure 8f) and the original color is not achieved. The same is true for C14S*n* and *n*-S-2-S-*n* even for Ag NPs where monomer adsorption is much stronger than desorption, and hence, no contrasting red color is achieved. Nevertheless, all titrations of Figures 1−3 clearly indicate a color change due to the change in the SPR response of both Ag and Au NPs, and hence, both kinds of NPs act as excellent indicators for the monomer/micelle−NP interactions.

CONCLUSIONS

The above results show a successful implementation of Ag/Au NPs as fine indicators for tracing Gemini surfactant interactions with NPs. A sharp color contrast for both Ag and Au NPs without using any external indicator precisely demonstrated the mechanism of how monomer/micelles adsorb on the NP surface. The strong polarity of the Gemini surfactant is the driving force for an effective adsorption, although polar head group modifications in the form of methylene and thio ether spacers leave a marked effect. The stronger the amphiphilicity of the Gemini surfactant, the greater the degree of its adsorption on the NP surface, and hence, the larger the monomer/micelle−NP aggregates are produced. Such an association entraps a large number of NPs, thus bringing a large shift from the singly dispersed colloidal NP state to an aggregated assembly, resulting in a sharp color contrast due to a change in the SPR response. It is precisely demonstrated by UV−visible and DLS measurements, suggesting a straightforward way of implementation of this methodology to determine monomer/micelle−NP interactions in complex media where strong amphiphilic molecules and their aggregated assemblies are frequently encountered by Ag/Au NPs.

ASSOCIATED CONTENT

Supporting Information

The Supporting Information is available free of charge at https://pubs.acs.org/doi/10.1021/acs.langmuir.2c00853.

Molecular formulas, UV−visible spectra, size and zeta potential profiles, IR spectra, XPS spectra, and data tables (PDF)

AUTHOR INFORMATION

Corresponding Author

Mandeep Singh Bakshi − *Department of Chemistry, Natural and Applied Sciences, University of Wisconsin−Green Bay, Green Bay, Wisconsin 54311-7001, United States;* orcid.org/0000-0003-1251-9590; Email: bakshim@uwgb.edu

Authors

Prabhjot Kaur − *Department of Chemistry, Natural and Applied Sciences, University of Wisconsin−Green Bay, Green Bay, Wisconsin 54311-7001, United States; Department of Chemistry, B.B.K. D.A.V. College for Women, Amritsar 143005 Punjab, India; Department of Chemistry, Dr. B.R. Ambedkar National Institute of Technology, Jalandhar 144011 Punjab, India*

Jaspreet Kaur Rajput − *Department of Chemistry, Dr. B.R. Ambedkar National Institute of Technology, Jalandhar 144011 Punjab, India*

Kultar Singh − *Department of Chemistry, Khalsa College, Amritsar 143002 Punjab, India*

Poonam Khullar − *Department of Chemistry, B.B.K. D.A.V. College for Women, Amritsar 143005 Punjab, India*

Complete contact information is available at: https://pubs.acs.org/10.1021/acs.langmuir.2c00853

Notes

The authors declare no competing financial interest.

ACKNOWLEDGMENTS

This research was supported by WiSys and University of Wisconsin System applied research funding (Ignite Grant for Applied Research, #FY22-106-068000-4). The views expressed herein are those of the authors and are not necessarily those of WiSys or the UW System.

REFERENCES

(1) Rodriguez-Fernandez, J.; Perez-Juste, J.; Mulvaney, P.; Liz-Marzan, L. M. Spatially-directed oxidation of gold nanoparticles by Au(III)-CTAB complexes. *J. Phys. Chem. B* **2005**, *109*, 14257−14261.

(2) Aguirre, C. M.; Kaspar, T. R.; Radloff, C.; Halas, N. J. CTAB Mediated Reshaping of Metallodielectric Nanoparticles. *Nano Lett.* **2003**, *3*, 1707−1711.

(3) Alkilany, A. M.; Murphy, C. J. Gold Nanoparticles With a Polymerizable Surfactant Bilayer: Synthesis, Polymerization, and Stability Evaluation. *Langmuir* **2009**, *25*, 13874−13879.

(4) Smith, D. K.; Miller, N. R.; Korgel, B. A. Iodide in CTAB Prevents Gold Nanorod Formation. *Langmuir* **2009**, *25*, 9518−9524.

(5) Kuo, C. H.; Chiang, T. F.; Chen, L. J.; Huang, M. H. Synthesis of Highly Faceted Pentagonal- and Hexagonal-Shaped Gold Nanoparticles With Controlled Sizes by Sodium Dodecyl Sulfate. *Langmuir* **2004**, *20*, 7820−7824.

(6) Hill, H. D.; Millstone, J. E.; Banholzer, M. J.; Mirkin, C. A. The Role Radius of Curvature Plays in Thiolated Oligonucleotide Loading on Gold Nanoparticles. *ACS Nano* **2009**, *3*, 418−424.

(7) Bakshi, M. S. How Surfactants Control Crystal Growth of Nanomaterials. *Cryst. Growth Des.* **2016**, *16*, 1104−1133.
(8) Bakshi, M. S.; Sachar, S.; Kaur, G.; Bhandari, P.; Kaur, G.; Biesinger, M. C.; Possmayer, F.; Petersen, N. O. Dependence of Crystal Growth of Gold Nanoparticles on the Capping Behavior of Surfactant at Ambient Conditions. *Cryst. Growth Des.* **2008**, *8*, 1713−1719.
(9) Lysyakova, L.; Lomadze, N.; Neher, D.; Maximova, K.; Kabashin, A. V.; Santer, S. Light-Tunable Plasmonic Nanoarchitectures Using Gold Nanoparticles-Azobenzene -Containing Cationic Surfactant Complexes. *J. Phys. Chem. C* **2015**, *119*, 3762−3770.
(10) Alkilany, A. M.; Nagaria, P. K.; Wyatt, M. D.; Murphy, C. J. Cation Exchange on the Surface of Gold Nanorods With a Polymerizable Surfactant: Polymerization, Stability, and Toxicity Evaluation. *Langmuir* **2010**, *26*, 9328−9333.
(11) Tiwari, A. K.; Sonu; Saha, S. K. Effect of Hydroxyl Group Substituted Spacer Group of Cationic Gemini Surfactants on Solvation Dynamics and Rotational Relaxation of Coumarin-480 in Aqueous Micelles. *J. Phys. Chem. B* **2014**, *118*, 3582−3592.
(12) Vijayaraghavan, P.; Liu, C. H.; Hwang, K. C. Synthesis of Multibranched Gold Nanoechinus Using a Gemini Cationic Surfactant and Its Application for Surface Enhanced Raman Scattering. *ACS Appl. Mater. Interfaces* **2016**, *8*, 23909−23919.
(13) Gomez-Grana, S.; Hubert, F.; Testard, F.; Guerrero-Martinez, A.; Grillo, I.; Liz-Marzan, L. M.; Spalla, O. Surfactant (Bi)Layers on Gold Nanorods. *Langmuir* **2012**, *28*, 1453−1459.
(14) Bakshi, M. S.; Possmayer, F.; Petersen, N. O. Aqueous-Phase Room-Temperature Synthesis of Gold Nanoribbons: Soft Template Effect of a Gemini Surfactant. *J. Phys. Chem. C* **2008**, *112*, 8259−8265.
(15) Aggrawal, R.; Halder, S.; Gopalan, B.; Biswas, S.; Saha, S. K. Transformation of an Aqueous Micellar Phase to a Bilayer of Gemini Surfactants on Gold Nanoparticles: A Steady-State and Time-Resolved Fluorescence and Fluorescence Anisotropy Study by Tuning the Precise Locations of Probes. *J. Phys. Chem. C* **2022**, *126*, 6280−6299.
(16) Riedesel, S.; Kaur, R.; Bakshi, M. S. Distinguishing Nanoparticle-Nanoparticle Interactions Between Gold and Silver Nanoparticles Controlled by Gemini Surfactants: Stability of Nanocolloids. *J. Phys. Chem. C* **2021**, *125*, 5399−5411.
(17) Kaur, R.; Singh, K.; Khullar, P.; Gupta, A.; Ahluwalia, G. K.; Bakshi, M. S. Applications of Molecular Structural Aspects of Gemini Surfactants in Reducing Nanoparticle-Nanoparticle Interactions. *Langmuir* **2019**, *35*, 14929−14938.
(18) Kang, H.; Buchman, J. T.; Rodriguez, R. S.; Ring, H. L.; He, J.; Bantz, K. C.; Haynes, C. L. Stabilization of Silver and Gold Nanoparticles: Preservation and Improvement of Plasmonic Functionalities. *Chem. Rev.* **2019**, *119*, 664−699.
(19) Alkilany, A. M.; Lohse, S. E.; Murphy, C. J. The Gold Standard: Gold Nanoparticle Libraries To Understand the Nano-Bio Interface. *Acc. Chem. Res.* **2013**, *46*, 650−661.
(20) Agarwal, V.; Gupta, V.; Bhardwaj, V. K.; Singh, K.; Khullar, P.; Bakshi, M. S. Hemolytic Response of Iron Oxide Magnetic Nanoparticles at the Interface and in Bulk: Extraction of Blood Cells by Magnetic Nanoparticles. *ACS Appl. Mater. Interfaces* **2022**, *14*, 6428−6441.
(21) Maus, L.; Dick, O.; Bading, H.; Spatz, J. P.; Fiammengo, R. Conjugation of Peptides to the Passivation Shell of Gold Nanoparticles for Targeting of Cell-Surface Receptors. *ACS Nano* **2010**, *4*, 6617−6628.
(22) Yi, M.; Ma, L.; Zhao, W.; Zhao, J.; Fan, Q.; Hao, J. Amphiphilic Au Nanoclusters Modulated by Magnetic Gemini Surfactants As a Cysteine Chemosensor and an MRI Contrast Agent. *Langmuir* **2021**, *37*, 3130−3138.
(23) Shaban, S. M.; Lee, J. Y.; Kim, D. H. Dual-Surfactant-Capped Ag Nanoparticles As a Highly Selective and Sensitive Colorimetric Sensor for Citrate Detection. *ACS Omega* **2020**, *5*, 10696−10703.
(24) Li, J. X.; Zhou, L. H.; Han, X.; Liu, H. L. Direct Electrochemistry of Hemoglobin Based on Gemini Surfactant Protected Gold Nanoparticles Modified Glassy Carbon Electrode. *Sens. Actuators, B* **2008**, *135*, 322−326.
(25) Ye, W.; Kruger, K.; Sanchez-Iglesias, A.; Garcia, I.; Jia, X.; Sutter, J.; Celiksoy, S.; Foerster, B.; Liz-Marzán, L. M.; Ahijado-Guzmán, R.; Sönnichsen, C. CTAB Stabilizes Silver on Gold Nanorods. *Chem. Mater.* **2020**, *32*, 1650−1656.
(26) Yu, D.; Yam, V. W.-W. Hydrothermal-Induced Assembly of Colloidal Silver Spheres into Various Nanoparticles on the Basis of HTAB-Modified Silver Mirror Reaction. *J. Phys. Chem. B* **2005**, *109*, 5497−5503.
(27) Xu, H.; Xu, J.; Jiang, X.; Zhu, Z.; Rao, J.; Yin, J.; Wu, T.; Liu, H.; Liu, S. Thermosensitive Unimolecular Micelles Surface-Decorated With Gold Nanoparticles of Tunable Spatial Distribution. *Chem. Mater.* **2007**, *19*, 2489−2494.
(28) Ray, D.; Kumar, S.; Aswal, V. K.; Kohlbrecher, J. Tuning Nanoparticle-Micelle Interactions and Resultant Phase Behavior. *Langmuir* **2018**, *34*, 259−267.
(29) Zhao, F.; Yang, W.; Shih, T.-M.; Feng, S.; Zhang, Y.; Li, J.; Yan, J.; Yang, Z. Plasmoelectric Potential Mapping of a Single Nanoparticle. *ACS Photonics* **2018**, *5*, 3519−3525.
(30) Sheldon, M. T.; van de Groep, J.; Brown, A. M.; Polman, A.; Atwater, H. A. Plasmoelectric potentials in metal nanostructures. *Science* **2014**, *346*, 828−831.
(31) Kohl, D.; Mesquida, P.; Schitter, G. Quantitative AC − Kelvin Probe Force Microscopy. *Microelectron. Eng.* **2017**, *176*, 28−32.
(32) Kabir, u. D.; Siddiqui, U. S.; Ghosh, G. Growth of Gemini Surfactant Micelles Under the Influence of Additives: DLS Studies. *J. Dispersion Sci. Technol.* **2009**, *30*, 1310−1319.
(33) Nakahara, H.; Nishizaka, H.; Iwasaki, K.; Otsuji, Y.; Sato, M.; Matsuoka, K.; Shibata, O. Role of the Spacer of Gemini Surfactants in Solubilization into Their Micelles. *J. Mol. Liq.* **2017**, *244*, 499−505.
(34) Bhut, P. R.; Pal, N.; Mandal, A. Characterization of Hydrophobically Modified Polyacrylamide in Mixed Polymer-Gemini Surfactant Systems for Enhanced Oil Recovery Application. *ACS Omega* **2019**, *4*, 20164−20177.
(35) Zhao, W.; Song, K.; Chen, Y.; Wang, H.; Liu, Z.; Shi, Q.; Huang, J.; Wang, Y. Aggregation of a Cationic Gemini Surfactant With a Chelating Molecule and Effects From Calcium Ions. *Langmuir* **2017**, *33*, 12719−12728.
(36) Bakshi, M. S.; Singh, J.; Singh, K.; Kaur, G. Mixed Micelles of Cationic 12-2-12 Gemini With Conventional Surfactants: the Head Group and Counterion Effects. *Colloids Surf., A* **2004**, *237*, 61−71.
(37) Yang, J.; Huang, H.; Zheng, J.; Huang, Y.; Xie, H.; Gao, F. Effect of Head Group of Surfactant on the Self-Assembly Structures and Aggregation Transitions in a Mixture of Cationic Surfactant and Anionic Surfactant-Like Ionic Liquid. *J. Mol. Liq.* **2020**, *308*, No. 112995.
(38) Linker, G. J.; van Duijnen, P. T.; Broer, R. Understanding Trends in Molecular Bond Angles. *J. Phys. Chem. A* **2020**, *124*, 1306−1311.
(39) Joodaki, F.; Martin, L. M.; Greenfield, M. L. Planarity and Out-of-Plane Vibrational Modes of Tryptophan and Tyrosine in Biomolecular Modeling. *Phys. Chem. Chem. Phys.* **2019**, *21*, 23943−23965.
(40) Banjare, M. K.; Kurrey, R.; Yadav, T.; Sinha, S.; Satnami, M. L.; Ghosh, K. K. A Comparative Study on the Effect of Imidazolium-Based Ionic Liquid on Self-Aggregation of Cationic, Anionic and Nonionic Surfactants Studied by Surface Tension, Conductivity, Fluorescence and FTIR Spectroscopy. *J. Mol. Liq.* **2017**, *241*, 622−632.
(41) Kolen'ko, Y. V.; Bañobre-Lopez, M.; Rodríguez-Abreu, C.; Carbó-Argibay, E.; Sailsman, A.; Piñeiro-Redondo, Y.; Cerqueira, M. F.; Petrovykh, D. Y.; Kovnir, K.; Lebedev, O. I.; Rivas, J. Large-Scale Synthesis of Colloidal Fe_3O_4 Nanoparticles Exhibiting High Heating Efficiency in Magnetic Hyperthermia. *J. Phys. Chem. C* **2014**, *118*, 8691−8701.
(42) Xie, C.; Yang, Q.; Xu, Z.; Liu, X.; Du, Y. New Route to Synthesize Highly Active Nanocrystalline Sulfated Titania-Silica:

https://doi.org/10.1021/acs.langmuir.2c00853
Langmuir 2022, 38, 7802−7814

Synergetic Effects Between Sulfate Species and Silica in Enhancing the Photocatalysis Efficiency. *J. Phys. Chem. B* **2006**, *110*, 8587−8592.
(43) Weng, L. T.; Bertrand, P.; Stone-Masui, J. H.; Stone, W. E. E. Desorption of Emulsifiers From Polystyrene Latexes Studied by Various Surface Techniques: A Comparison Between XPS, ISS, and Static SIMS. *Langmuir* **1997**, *13*, 2943−2952.
(44) Krozer, A.; Rodahl, M. X-ray photoemission spectroscopy study of UV/ozone oxidation of Au under ultrahigh vacuum conditions. *J. Vac. Sci. Technol., A* **1997**, *15*, 1704.
(45) Siril, P. F.; Shiju, N. R.; Brown, D. R.; Wilson, K. Optimising Catalytic Properties of Supported Sulfonic Acid Catalysts. *Appl. Catal., A* **2009**, *364*, 95−100.
(46) Hwang, J.; Lee, D. G.; Yeo, H.; Rao, J.; Zhu, Z.; Shin, J.; Jeong, K.; Kim, S.; Jung, H. W.; Khan, A. Proton Transfer Hydrogels: Versatility and Applications. *J. Am. Chem. Soc.* **2018**, *140*, 6700−6709.
(47) Battocchio, C.; Porcaro, F.; Mukherjee, S.; Magnano, E.; Nappini, S.; Fratoddi, I.; Quintiliani, M.; Russo, M. V.; Polzonetti, G. Gold nanoparticles stabilized with aromatic thiols: Interaction at the molecule−metal interfaceand ligand arrangement in the molecular shell investigated by SR-XPS and NEXAFS. *J. Phys. Chem. C* **2014**, *118*, 8159−8168.
(48) Casanovas, J.; Ricart, J. M.; Rubio, J.; Illas, F.; Jiménez-Mateos, J. M. Origin of the Large N 1s Binding Energy in X-Ray Photoelectron Spectra of Calcined Carbonaceous Materials. *J. Am. Chem. Soc.* **1996**, *118*, 8071−8076.
(49) Watanabe, M.; Ando, H.; Handa, T.; Ichino, T.; Kuwaki, N. Comparative XPS Study of Silver and Copper Surfaces Exposed to Flowing Air Containing Low Concentration of Sulfur Dioxide. *Zairyo-to-Kankyo* **2007**, *56*, 10−15.

https://doi.org/10.1021/acs.langmuir.2c00853
Langmuir 2022, 38, 7802−7814